

# Participatory Horizons and the CMB Parity Anomaly: A Smoothed Antipodal Evidence Operator

Gregory O’Grady\*

April 28, 2026

## Abstract

The  $\Lambda$ CDM model accounts for the cosmic microwave background with remarkable precision, yet persistent anomalies at the largest angular scales remain unexplained. Among these, the low-multipole temperature spectrum exhibits an even/odd parity asymmetry at the 0.2–0.3% level across  $\ell \lesssim 30$ . This programme hypothesises that such anomalies reflect the observer’s causal diamond acting as a recording aperture on the observed sky, while retaining  $\Lambda$ CDM as the underlying cosmology.

Companion papers derived an angular recording filter, a radial kernel, and a variance decoder from the ‘Participatory Modular Hamiltonian (PMH)’. The angular filter demonstrated it can resolve the low-power anomaly and the decoder reproduces the quadrupole–octopole alignment, but both channels record only unsigned threshold events and are provably parity-even. Here we show that all local recording-rate mechanisms are blocked from producing parity asymmetry by an exact spherical-harmonic identity, and that the rotationally covariant evasion within the present scalar pairing framework is a nonlocal antipodal kernel for which  $P_\ell(-1) = (-1)^\ell$  preserves the parity sign. Three structural principles, namely the antipodal pairing map, the negative sign from evidence optimality, and a heat-kernel smoothing envelope, fix the form of the operator; a geometric scale closure then reduces the model to a single fitted parameter, the contrast amplitude  $\rho$ .

The one-parameter model gives  $2\Delta \ln \mathcal{L} = 5.6$  over  $\Lambda$ CDM ( $\Delta\chi^2 = -7.4$ ;  $\Delta\text{AIC} = -3.6$ ). The geometric closure retains nearly the full likelihood of the freely fitted model, losing only  $\Delta(2\ln \mathcal{L}) \simeq 0.28$  while reducing the fit from three parameters to one. The parity ratio anomaly moves from the 1–3% tail to the 26–54% bulk at every tested  $\ell_{\text{max}}$ , and the  $S_{1/2}$  resolution of the angular filter is preserved.

The extended unified model is favoured over  $\Lambda$ CDM by information criteria in its present construction. However, the contrast amplitude  $\rho = 0.27$  remains a single fitted parameter. Resolving the programme’s amplitude gap from first principles remains the framework’s central open problem.

## 1 Introduction

The  $\Lambda$ CDM model provides a thoroughly tested account of the cosmic microwave background [1, 2], yet persistent anomalies at the largest angular scales remain unexplained [3–5]. Among these is the parity asymmetry of the low- $\ell$  temperature power spectrum, with odd multipoles systematically carrying more power than their even neighbours.

In WMAP data, this parity ratio  $R(\ell_{\text{max}}) = D^+/D^-$  was reported as anomalous at the 99.6% level for  $\ell = 2\text{--}18$  [6], later confirmed at the 0.2–0.3% level for  $\ell_{\text{max}} \approx 28$  by Planck [7, 8], and persisting in recent PR4 analyses [5, 8]. The anomaly is driven by the lowest multipoles,

---

\*Professor, University of Auckland, New Zealand. Parts of the computational workflow and manuscript preparation used AI-assisted tools under human oversight.

particularly  $\ell = 2-7$ , where individual even- $\ell$  powers fall systematically below  $\Lambda$ CDM while their odd neighbours do not, with the cumulative parity ratio reaching its most anomalous values by  $\ell_{\max} \approx 18-28$  before dilution by higher multipoles [4, 9]. The anomaly is distinct from the low-power deficit captured by  $S_{1/2}$  [10, 11] and from the quadrupole–octopole alignment [12–14], and concerns the alternating pattern of the spectrum rather than its overall amplitude or directional structure.

No consensus explanation for the parity anomaly has emerged. Statistical variability is reasonably invoked, while other proposed approaches modify the primordial spectrum or inflationary sector, including compact topologies, infrared cutoffs in the primordial power spectrum, loop quantum cosmology, and modified inflationary vacuum states [15–18]. The current programme evaluates an alternative hypothesis, rooted in a longstanding line of quantum thought, that the observer’s causal boundary participates in the measurement chain that determines which correlations become definite classical records [19–21]. The  $\Lambda$ CDM primordial spectrum and background cosmology are retained, while the anomalies are attributed to the recording process itself, not to new physics at early times.

Earlier papers developed this idea sector-by-sector with treatments of the low-power, alignment and cosmic dipole anomalies [22–27]. A companion triplet of papers then proceeded to place the programme on a more rigorous systematic footing. The first derived the Participatory Modular Hamiltonian (PMH); a conjugate pair of modular operators for the observer’s causal diamond, constructed from the Casini–Huerta–Myers modular Hamiltonian of a spherical region [28, 29], and yielding an angular recording filter  $h^2(\ell) = 1 - \exp[-\ell(\ell+1)/\ell_c^2]$  with  $\ell_c^2 = 12.56$  and a radial kernel. The recording prescription was then grounded in Lindblad dynamics [30], and a variance decoder with exact  $\kappa_{\ell m}$  coefficients was derived, together with a parity selection rule. Notably, however, this decoder was antipodally symmetric and cannot generate even/odd  $C_\ell$  asymmetry [31]. The angular filter resolves the low-power anomaly, shifting  $S_{1/2}$  from the 8th to the 50th percentile [26], and the decoder reproduces the observed quadrupole–octopole alignment, with a substantial amplitude gap remaining an open problem [31]. But neither channel touches the parity ratio.

The present paper addresses this gap. We show that a signed antipodal evidence channel, derived from three structural principles of the recording architecture, produces an even/odd  $C_\ell$  seesaw controlled by a single amplitude parameter  $\rho$ , with  $2\Delta \ln \mathcal{L} = 5.6$  as a descriptive score relative to  $\Lambda$ CDM,  $\Delta \text{AIC} = -3.6$ , and  $\Delta \text{BIC} = -2.2$ . The value of  $\rho$  is currently fitted; deriving recording amplitudes from first principles remains the fundamental open problem across all levels of the programme’s hierarchy.

## 2 Conceptual framework

The PMH architecture records the sky through three layers: an angular filter that suppresses the largest modes, a quantum monitoring process governed by Lindblad dynamics, and a variance decoder that maps the monitoring outcomes to sky coefficients [29–31]. The underlying collapse operator is linear in the local fluctuation and carries its sign. However, the canonical recording event is binary. A cell fires when the fluctuation exceeds a threshold, regardless of sign, so the firing probability is quadratic in the local signal — the linear term is absent. The resulting record is therefore antipodally symmetric,  $\pi(\hat{n}) = \pi(-\hat{n})$ , and no diagonal even/odd  $C_\ell$  asymmetry can arise from the unsigned channel alone.

The parity anomaly therefore requires consideration of a different retained variable as an architecture extension: the *signed* evidence contrast across a diameter of the causal diamond. This concept is outlined in schematic form in Figure 1, and is developed in detail here.

## 2.1 The local obstruction

The parity anomaly requires a mechanism that distinguishes even from odd  $\ell$  in the angular power spectrum  $C_\ell = (2\ell + 1)^{-1} \sum_m |a_{\ell m}|^2$ . Because  $C_\ell$  is a rotationally invariant ( $L = 0$ ) quantity obtained by summing over all  $m$ , any mechanism that modifies it must survive that sum.

Consider a local directional modulation of the recording rate,  $\Gamma(\hat{n})$ , with arbitrary angular structure. Its effect on  $C_\ell$  is proportional to

$$\sum_m |Y_{\ell m}(\hat{n})|^2 = \frac{2\ell + 1}{4\pi}, \quad (1)$$

which is the addition theorem for spherical harmonics. The right-hand side is independent of  $\hat{n}$  and independent of whether  $\ell$  is even or odd. Any local modulation  $\Gamma(\hat{n})$ , integrated against this sum, produces a multiplicative correction to  $C_\ell$  that depends on  $\ell$  only through the prefactor  $(2\ell + 1)/(4\pi)$  and therefore cannot distinguish even from odd multipoles. This is the local obstruction.

The result is not restricted to smooth or dipolar modulations. Ten alternative local mechanisms tested during the programme’s development, including chiral extensions at first and second order, cascade couplings between adjacent  $\ell$ , and boost-weighted contrasts, are all blocked by either the identity (1), one of three independent linear obstructions on odd kernels, or the  $M = 0$  confinement theorem.

The evasion requires a *nonlocal* kernel coupling  $\hat{n}$  to  $-\hat{n}$ . For such a kernel, the relevant sum becomes

$$\sum_m Y_{\ell m}(\hat{n}) Y_{\ell m}^*(-\hat{n}) = \frac{2\ell + 1}{4\pi} P_\ell(-1) = \frac{2\ell + 1}{4\pi} (-1)^\ell, \quad (2)$$

where  $P_\ell(-1) = (-1)^\ell$  is exact. The parity sign  $(-1)^\ell$  now survives the  $m$ -sum. An antipodal kernel modifies the probability that mode  $\ell$  is recorded, and the parity factor enters the power spectrum directly, unlike a local modulation which is erased by the summation over  $m$ . A nonlocal antipodal coupling is therefore the unique route to even/odd  $C_\ell$  asymmetry that preserves rotational covariance.

## 2.2 The antipodal evidence operator

The previous subsection established that no local scalar diagonal recording-rate mechanisms can produce even/odd  $C_\ell$  asymmetry, and that the unique evasion is a nonlocal antipodal kernel. We now describe the physical mechanism that connects such a kernel to the physics of the causal diamond, before deriving the specific operator.

The programme’s PMH/Lindblad architecture records whether local modular-energy fluctuations cross a threshold [30, 31]. This unsigned channel is quadratic in the local signal and therefore erases the sign of the fluctuation: it cannot distinguish a pattern from its antipodal reflection. But the underlying Lindblad collapse operator  $\hat{R}_a$  is *linear* in the modular-energy fluctuation — it carries its sign [30]. The signed information is physically present in the post-collapse quantum state and in the continuous quantum measurement current  $dY(\hat{n})$ ; the canonical decoder simply discards it [31].

The spherical causal diamond supplies a natural antipodal pairing of boundary directions. In the Casini–Huerta–Myers construction, the modular Hamiltonian of a ball-shaped region is geometrically tied to the diamond’s conformal structure, and the associated modular conjugation relates opposite boundary generators as the two ends of the same diameter [28]. This pairing is an intrinsic property of any spherical causal diamond and does not require the observer to be in motion. The Lindblad measurement itself remains local: each endpoint independently produces a signed measurement current. The nonlocal step occurs only after these

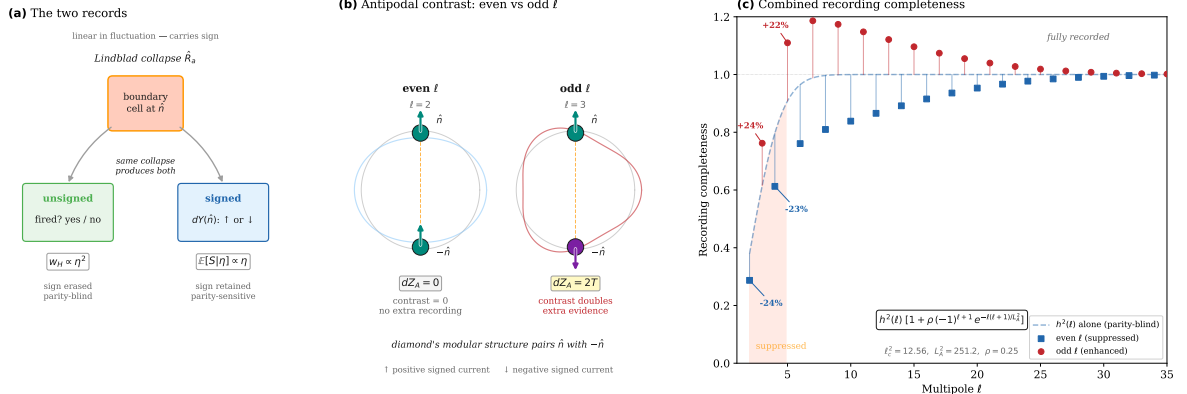


**Figure 1: Physical mechanism of the antipodal parity channel.** (a) The two records produced by a single Lindblad collapse event. The collapse operator  $\hat{R}_a$  is linear in the local modular-energy fluctuation and carries its sign. The canonical unsigned record (left, green) retains only whether the cell fired; its firing probability  $w_H \propto \eta^2$  erases the sign and is parity-blind. The signed measurement current  $dY(\hat{n})$  (right, blue) retains the sign and is parity-sensitive. (b) Antipodal contrast for even and odd  $\ell$ . The diamond's modular structure pairs each boundary direction  $\hat{n}$  with its antipode  $-\hat{n}$ . For an even- $\ell$  mode ( $\ell = 2$ , left), the signed currents at the two ends point the same way; the contrast  $dZ_A = dY(\hat{n}) - dY(-\hat{n})$  vanishes and no extra evidence is gained. For an odd- $\ell$  mode ( $\ell = 3$ , right), the signed currents point opposite ways; the contrast doubles the signal, providing an additional evidence channel. (c) Combined recording completeness  $h^2(\ell) [1 + \rho(-1)^{\ell+1} e^{-\ell(\ell+1)/L_A^2}]$  at the geometric values  $\ell_c^2 = 12.56$ ,  $L_A^2 = 251.2$ ,  $\rho = 0.27$ . Even multipoles (blue squares) are suppressed below the parity-blind baseline  $h^2(\ell)$  (dashed); odd multipoles (red circles) are enhanced above it. The seesaw decays with  $\ell$  as the heat-kernel envelope falls off, reflecting the finite angular resolution of the antipodal comparison. Percentage labels indicate the enhancement or suppression relative to  $h^2(\ell)$  alone at  $\ell = 2-5$ .

local currents have become classical records, when the evidence register forms the smoothed antipodal contrast (Section 2.4).

Because spherical harmonics satisfy  $Y_{\ell m}(-\hat{n}) = (-1)^\ell Y_{\ell m}(\hat{n})$ , the contrast channel cancels even- $\ell$  modes (which are antipodally symmetric) and doubles odd- $\ell$  modes (which are anti-symmetric) (Figure 1). Odd- $\ell$  modes therefore possess an additional signed evidence channel beyond the canonical unsigned one, while even- $\ell$  modes do not. The parity anomaly arises because the causal diamond records not only local threshold events but also finite-resolution signed contrast between the two ends of each diameter.

We now derive the specific form of the operator.

**Operator statement.** The diagonal parity modulation

$$C_\ell \mapsto \left[ 1 + \rho(-1)^{\ell+1} e^{-\ell(\ell+1)/L_A^2} \right] C_\ell \quad (3)$$

is equivalent to adding the recording operator

$$\mathcal{O}_A = -\rho e^{\Delta_{S^2}/L_A^2} \mathcal{P}, \quad (4)$$

where  $\mathcal{P}$  is the antipodal map  $(\mathcal{P}T)(\hat{n}) = T(-\hat{n})$  and  $e^{\Delta_{S^2}/L_A^2}$  is the spherical heat kernel at diffusion time  $t = 1/L_A^2$ . This follows immediately from  $\mathcal{P}Y_{\ell m} = (-1)^\ell Y_{\ell m}$  and  $e^{t\Delta_{S^2}} Y_{\ell m} =$

$e^{-t\ell(\ell+1)} Y_{\ell m}$ :

$$\mathcal{O}_A Y_{\ell m} = -\rho (-1)^\ell e^{-\ell(\ell+1)/L_A^2} Y_{\ell m} = \rho (-1)^{\ell+1} e^{-\ell(\ell+1)/L_A^2} Y_{\ell m}. \quad (5)$$

The operator  $\mathcal{O}_A$  is a recording-completeness or covariance-weight operator, not an amplitude-level operator acting directly on the temperature field. Its eigenvalues therefore enter the recorded power spectrum linearly. An amplitude-level sky-map operator would instead enter quadratically through  $|1 + \lambda_\ell|^2$ .

Three structural principles fix the three components of this operator, being the pairing map, the sign, and the smoothing envelope, leaving only the amplitude  $\rho$  and the scale  $L_A^2$  undetermined.

**The pairing map is unique.** A nonlocal evidence-pairing map  $\Pi : S^2 \rightarrow S^2$  that is (i) observer-centred, (ii) rotationally covariant, and (iii) involutive ( $\Pi^2 = \text{id}$ ) has exactly two solutions:  $\Pi = \text{id}$  (trivial, no nonlocal comparison) and  $\Pi = \mathcal{P}$  (antipodal). The identity gives no parity effect. Therefore  $\mathcal{P}$  is the unique choice.

**The sign is fixed by evidence optimality.** For a diameter pair of cells at  $\hat{n}$  and  $-\hat{n}$ , the local measurement currents decompose into common mode  $\mu_c = (\mu_+ + \mu_-)/2$  and contrast  $\mu_d = (\mu_+ - \mu_-)/2$ . The common mode is a nuisance degree of freedom representing background signal. The contrast is the score for endpoint distinguishability — the information that identifies structure along the diameter. The evidence-optimal statistic, the likelihood-ratio score for  $\mu_d$  after marginalising  $\mu_c$ , is proportional to  $dY(\hat{n}) - dY(-\hat{n})$ . In operator form this is  $1 - \mathcal{P}$ , which enhances odd- $\ell$  modes (eigenvalue  $+2$  under  $1 - \mathcal{P}$ ) and suppresses even- $\ell$  modes (eigenvalue  $0$ ), fixing the negative sign in  $\mathcal{O}_A = -\rho H_t \mathcal{P}$ . This is consistent with the observed enhancement of odd modes; the common-mode alternative  $1 + \mathcal{P}$  would worsen the anomaly.

After normalising the total recording completeness around the parity-blind baseline, this contrast channel is represented as a seesaw modulation proportional to  $-\mathcal{P}$ : even modes are suppressed relative to baseline and odd modes enhanced (Figure 1).

**The smoothing envelope is the heat kernel.** A rotationally covariant smoothing operator on  $S^2$  is diagonal in spherical harmonics:  $H_t Y_{\ell m} = h_\ell(t) Y_{\ell m}$ . If the smoothing is Markovian, i.e.,  $H_{t_1} H_{t_2} = H_{t_1+t_2}$ , the eigenvalues form a semigroup:  $h_\ell(t) = e^{-\lambda_\ell t}$ . If the generator is local and second-order, rotational covariance on  $S^2$  fixes it uniquely to the spherical Laplacian, giving  $\lambda_\ell = \ell(\ell+1)$  and hence  $H_t = e^{t\Delta_{S^2}}$ , the spherical heat semigroup. No free functional choice remains; the smoothing envelope is  $e^{-\ell(\ell+1)/L_A^2}$  with a single scale parameter  $L_A^2 = 1/t$ .

**Combined recording model.** The full recorded power spectrum is

$$\boxed{C_\ell^{\text{rec}} = h^2(\ell; \ell_c^2) \left[ 1 + \rho (-1)^{\ell+1} e^{-\ell(\ell+1)/L_A^2} \right] C_\ell^{\text{ACDM}}}, \quad (6)$$

where  $h^2(\ell; \ell_c^2) = 1 - \exp[-\ell(\ell+1)/\ell_c^2]$  is the angular recording filter from the PMH framework [26, 29], acting on the isotropic power, and the square bracket is the parity modulation from the antipodal evidence operator.

**Recording-completeness interpretation.** The angular filter  $h^2(\ell)$  and the radial kernel together measure how completely mode  $\ell$  is recorded by the unsigned channel, being the count of independent recording opportunities across angular sectors and radial depth [26, 29].

The parity modulation adds a second, independent source of classical evidence, the signed antipodal contrast. Odd- $\ell$  modes, which produce nonzero contrast ( $[1 - (-1)^\ell] = 2$ ), are visible to both channels and are therefore recorded more completely. Even- $\ell$  modes, which produce zero contrast ( $[1 - (-1)^\ell] = 0$ ), are visible only to the unsigned channel and receive no enhancement. The heat-kernel envelope  $e^{-\ell(\ell+1)/L_A^2}$  encodes the finite angular resolution of the antipodal comparison, ensuring that the parity modulation decays at high  $\ell$ .

**Real-space interpretation.** The kernel  $K_A(\hat{n}, \hat{n}') = -\rho H_t(\hat{n}, -\hat{n}')$  defines a blurred patch of angular radius  $\sigma_A = \sqrt{2/L_A^2} \simeq 5.1^\circ$  (FWHM  $\simeq 12.0^\circ$ ) centred on the antipodal point  $-\hat{n}$ . The negative sign means that the recording process preferentially retains smoothed antipodal contrast,  $T(\hat{n}) - T(-\hat{n})$ , over antipodal common mode,  $T(\hat{n}) + T(-\hat{n})$ .

**Positivity.** For  $\rho = 0.272$  and  $L_A^2 = 251.2$ , the most negative modulation over  $\ell \geq 2$  occurs at  $\ell = 2$ :

$$1 - \rho e^{-6/L_A^2} \simeq 1 - 0.272 e^{-6/251.2} \simeq 0.734 > 0.$$

The modulation envelope decreases with  $\ell$ , so all higher even multipoles are less strongly suppressed. The modified covariance is therefore positive-semidefinite for all  $\ell \geq 2$ .

### 2.3 Geometric scale closure

In a free three-parameter fit (Section 4), the preferred antipodal smoothing scale is  $L_A^2 \simeq 250$ . The PMH framework independently predicts  $\ell_c^2 = 12.56$  from the ratio of the conformal time to the comoving distance to last scattering [26, 29]. The relation

$$L_A^2 = d(d+1) \ell_c^2 = 20 \times 12.56 = 251.2 \quad (d=4) \quad (7)$$

lies within the broad likelihood plateau of the free fit and costs only  $\Delta(2 \ln \mathcal{L}) \simeq 0.28$  relative to the three-parameter model. The factor  $d(d+1) = 20$  in  $d = 4$  spacetime dimensions corresponds to the number of endpoint-resolved modular-evidence channels available to a diameter-pair comparison.

Adopting this closure reduces the model to a single fitted parameter: the contrast amplitude  $\rho$ . The numerical match is close and the dimensional counting is plausible, but absent a derivation from the microscopic dynamics the closure remains a hypothesis.

### 2.4 Nonlocality resolution

The operator  $\mathcal{O}_A$  couples  $\hat{n}$  to  $-\hat{n}$ , which appears to conflict with the local Lindblad dynamics presented previously [30]. The resolution rests on separating three distinct operations: the local quantum measurement, the geometric pairing, and the classical comparison.

**Layer 2a: local quantum monitoring (unchanged).** Each cell on the causal diamond boundary produces a local measurement current

$$dY(\hat{n}, t) = \sqrt{2\kappa} \mu(\hat{n}, t) dt + dW(\hat{n}, t), \quad (8)$$

where  $\mu(\hat{n}, t) = \text{Tr}[\hat{R}(\hat{n}) \rho_c(t)]$  is the conditional expectation of the collapse operator. This current is linear in the local modular-energy fluctuation and carries its sign. The measurement is entirely local and Lindblad-compatible.

**The geometric pairing.** The diamond does not send a signal from one side of the sky to the other. It defines a geometrically natural pairing of opposite boundary directions: in the Casini–Huerta–Myers construction, the modular structure of a ball-shaped region singles out antipodal boundary points as the two ends of the same diameter [28]. This pairing is a property of the diamond’s conformal geometry, not a dynamical process.

**Classical evidence processing.** Once local quantum monitoring has written signed measurement currents into classical registers at each endpoint, the evidence register forms the smoothed antipodal contrast

$$dZ_A(\hat{n}, t) = H_{t/2} dY(\hat{n}, t) - H_{t/2} dY(-\hat{n}, t). \quad (9)$$

This is subtraction of two classical numbers. Each boundary cell undergoes quantum measurement independently; the antipodal subtraction acts only on the resulting classical records.

**Compatibility with the decoder parity rule.** The parity selection rule previously induced [31] applies to the hazard-only record, where the firing probability  $w_H(\eta) \propto \eta^2$  is even and the signed information is discarded. The antipodal operator arises from the extended record that retains the signed measurement currents. There is no contradiction as the canonical triplet and the antipodal extension draw on different components of the same Lindblad dynamics, i.e., the unsigned hazard and the signed evidence respectively.

### 3 Methods and numerical implementation

#### 3.1 Baseline spectrum and Planck data

The fiducial  $\Lambda$ CDM power spectra are computed with CAMB [32] using the Planck 2018 best-fit parameters:  $H_0 = 67.36 \text{ km s}^{-1} \text{ Mpc}^{-1}$ ,  $\Omega_b h^2 = 0.02237$ ,  $\Omega_c h^2 = 0.1200$ ,  $\tau = 0.054$ ,  $n_s = 0.9649$ ,  $A_s = 2.1 \times 10^{-9}$  [2]. Lensing is disabled and the accuracy boost is set to 2.0 to ensure convergence at the lowest multipoles. The code returns the unlensed scalar  $D_\ell \equiv \ell(\ell+1) C_\ell / (2\pi)$  in  $\mu\text{K}^2$  for TT from  $\ell = 2$  to  $\ell = 2500$ . From the same run we extract the conformal time to the present  $\eta_0$  and the comoving distance to last scattering  $\chi_\star$ ; these enter the geometric predictions of Section 2.3.

The observed TT bandpowers are taken from the Planck 2018 public release<sup>1</sup>. At each multipole the quoted asymmetric error bars are symmetrised as  $\sigma_\ell = \frac{1}{2}(|\sigma_\ell^+| + |\sigma_\ell^-|)$ ; these are used for the supplementary  $\chi^2$  diagnostic and for plotting, while the primary likelihood uses the scaled- $\chi^2$  distribution directly. The fitting range is  $2 \leq \ell \leq 30$ , encompassing the multipoles where both the angular filter and the parity modulation produce appreciable effects.

#### 3.2 Combined recording model

The filtered temperature spectrum is

$$D_\ell^{\text{rec}} = h^2(\ell; \ell_c^2) \left[ 1 + \rho (-1)^{\ell+1} e^{-\ell(\ell+1)/L_A^2} \right] D_\ell^{\Lambda\text{CDM}}, \quad (10)$$

with  $h^2(\ell; \ell_c^2) = 1 - \exp[-\ell(\ell+1)/\ell_c^2]$ . The model is evaluated in four configurations to assess the cost of fixing each scale parameter from geometry:

(A) **Best-fit (3 parameters):**  $\ell_c^2$ ,  $\rho$ ,  $L_A^2$  all fitted.

---

<sup>1</sup>COM.PowerSpect.CMB-TT-full1.R3.01.txt, available from the Planck Legacy Archive.

- (B) **Geometric  $\ell_c^2$  (2 parameters)**:  $\ell_c^2 = 12.56$  fixed from horizon geometry;  $\rho$  and  $L_A^2$  fitted.
- (C) **FRW refined (2 parameters)**:  $\ell_c^2 = 13.01$  from the refined FRW calculation;  $\rho$  and  $L_A^2$  fitted.
- (D) **Geometric closure (1 parameter)**:  $\ell_c^2 = 12.56$  and  $L_A^2 = d(d+1)\ell_c^2 = 251.2$  both fixed; only  $\rho$  fitted.

Configuration (D) is the headline model. Configurations (A)–(C) serve as controls, quantifying the likelihood cost, if any, of imposing the geometric constraints.

### 3.3 Low- $\ell$ likelihood

At low multipoles the power-spectrum estimator follows  $\hat{D}_\ell = D_\ell^{\text{th}} \chi_{\nu_\ell}^2 / \nu_\ell$ , where  $\nu_\ell = f_{\text{sky}}(2\ell+1)$  effective degrees of freedom and  $f_{\text{sky}} = 0.86$  corresponds to the Commander confidence mask [2]. The per-multipole log-likelihood, up to constants independent of the model, is

$$\ln \mathcal{L}_\ell = -\frac{\nu_\ell}{2} \ln D_\ell^{\text{th}} - \frac{\nu_\ell D_\ell^{\text{obs}}}{2 D_\ell^{\text{th}}}, \quad (11)$$

summed over  $2 \leq \ell \leq 30$ . Parameters are scanned on fine grids:  $\ell_c^2$  from 5 to 40 in 351 steps when free;  $L_A^2$  from 20 to 1000 in 393 steps when free;  $\rho$  from 0 to 0.90 in 451 steps in all configurations. The best-fit is the grid point maximising the total log-likelihood, and the improvement over  $\Lambda$ CDM is reported as  $2\Delta \ln \mathcal{L}$ . The comparison with  $\Lambda$ CDM is reported as a descriptive model-score improvement, since the recording model does not reduce to  $\Lambda$ CDM when  $\rho = 0$ . The nested test within the recording framework compares the  $h^2$ -only model with the  $h^2 + \rho$  antipodal model at fixed geometric scales. Since  $\rho \geq 0$  is a boundary parameter, the quoted  $p$ -value uses the standard Chernoff boundary mixture rather than an ordinary  $\chi_1^2$  Wilks test. Information criteria are computed as  $\text{AIC} = -2\ln \mathcal{L}_{\text{max}} + 2k$  and  $\text{BIC} = -2\ln \mathcal{L}_{\text{max}} + k \ln N$ , where  $k$  is the number of fitted parameters and  $N = 29$  is the number of multipoles. A supplementary  $\Delta\chi^2$  statistic using the symmetrised bandpower errors is also reported; it uses the Gaussian residual  $(D_\ell^{\text{obs}} - D_\ell^{\text{th}})^2 / \sigma_\ell^2$  and is independent of the likelihood form.

### 3.4 Parity ratio diagnostic

The parity ratio is defined following Kim et al [9]:

$$R(\ell_{\text{max}}) = \frac{\sum_{\ell \text{ even}} D_\ell}{\sum_{\ell \text{ odd}} D_\ell}, \quad (12)$$

summed over  $2 \leq \ell \leq \ell_{\text{max}}$ . For each model and each  $\ell_{\text{max}} \in \{5, 7, 10, 15, 20, 22, 25, 30\}$ , we generate 200,000 Monte Carlo realisations by drawing  $\hat{D}_\ell = D_\ell^{\text{th}} \chi_{\nu_\ell}^2 / \nu_\ell$  at each multipole with  $\nu_\ell = f_{\text{sky}}(2\ell+1)$  degrees of freedom and the appropriate theoretical  $D_\ell^{\text{th}}$  (either unmodified  $\Lambda$ CDM or the model). The lower-tail probability  $P(R < R_{\text{obs}})$  is computed for the Planck-observed parity ratio at each  $\ell_{\text{max}}$ . The anomaly is considered resolved when the observed ratio moves from the tail ( $P \lesssim 5\%$ ) to the bulk ( $P \sim 20\text{--}50\%$ ).

### 3.5 $S_{1/2}$ diagnostic

The two-point angular correlation function and the  $S_{1/2}$  statistic are computed following the same procedure as in the angular filter paper [26]. Briefly,

$$C(\theta) = \sum_\ell \frac{2\ell+1}{4\pi} C_\ell P_\ell(\cos \theta) \quad (13)$$



is evaluated on a grid of 720 uniformly spaced angles, and

$$S_{1/2} = \int_{60^\circ}^{180^\circ} [C(\theta)]^2 \sin \theta d\theta \quad (14)$$

is computed by the trapezoidal rule. Planck bandpower-derived  $S_{1/2}$  within 10,000 Monte Carlo realisations of each model is reported, verifying that the parity extension does not disturb the  $S_{1/2}$  resolution achieved by the angular filter alone.

## 4 Results

### 4.1 Model comparison

Table 1 summarises the four configurations. The fully free three-parameter model gives  $2\Delta \ln \mathcal{L} = 5.89$  relative to  $\Lambda$ CDM as a descriptive score. The one-parameter geometric-closure model gives  $2\Delta \ln \mathcal{L} = 5.61$ , losing only  $\Delta(2 \ln \mathcal{L}) = 0.28$  while reducing the number of fitted parameters from three to one. It therefore has the strongest information-criterion performance, with  $\Delta \text{AIC} = -3.6$  and  $\Delta \text{BIC} = -2.2$  relative to  $\Lambda$ CDM. Conditional on the recording framework, the nested comparison between the  $h^2$ -only model and the antipodal extension gives  $2\Delta \ln \mathcal{L} = 4.09$  for the non-negative amplitude parameter  $\rho$ , corresponding to a boundary-mixture  $p = 0.022$ .

Table 1: Model comparison against Planck TT bandpowers ( $\ell = 2\text{--}30$ ,  $f_{\text{sky}} = 0.86$ ). Configurations differ in which parameters are fitted (f) versus derived from geometry (g).  $2\Delta \ln \mathcal{L}$ ,  $\Delta \chi^2$ ,  $\Delta \text{AIC}$  are relative to  $\Lambda$ CDM (negative = favoured). Configuration D is the headline result.

Config.	$\ell_c^2$	$\rho$	$L_A^2$	$k$	$2\Delta \ln \mathcal{L}$	$\Delta \chi^2$	$\Delta \text{AIC}$
$\Lambda$ CDM	—	—	—	0	0	0	0
(A) 3-param	9.40 <sup>f</sup>	0.300	217.5 <sup>f</sup>	3	5.89	−7.39	+0.1
(B) 2-param	12.56 <sup>g</sup>	0.280	235.0 <sup>f</sup>	2	5.61	−7.40	−1.6
(C) 2-param (FRW)	13.01 <sup>g</sup>	0.278	237.5 <sup>f</sup>	2	5.53	−7.39	−1.5
<b>(D) 1-param</b>	<b>12.56<sup>g</sup></b>	<b>0.272</b>	<b>251.2<sup>g</sup></b>	<b>1</b>	<b>5.61</b>	<b>−7.41</b>	<b>−3.6</b>

### 4.2 Temperature power spectrum

Figure 2 shows the low- $\ell$  TT spectrum for the geometric-closure model (configuration D) against Planck 2018 bandpowers. The model produces the characteristic even/odd seesaw visible in the data: even multipoles are pulled down relative to  $\Lambda$ CDM and odd multipoles are pushed up. The angular recording filter  $h^2(\ell)$  simultaneously suppresses  $\ell = 2\text{--}3$ , so that the combined model addresses both the low-power deficit and the parity asymmetry within a single recorded spectrum.

### 4.3 Parity ratio resolution

Table 2 reports the lower-tail probability  $P(R < R_{\text{obs}})$  at each  $\ell_{\text{max}}$  under  $\Lambda$ CDM and under the geometric-closure model, from 200,000 Monte Carlo realisations. Under  $\Lambda$ CDM, the Planck-observed parity ratio sits in the 0.7–4.5% tail at every  $\ell_{\text{max}}$  tested. Under the model, the same observed values sit in the 26–54% range, squarely in the bulk of the distribution. The parity anomaly is resolved at all  $\ell_{\text{max}}$  simultaneously.

Figure 3 shows the parity ratio as a function of  $\ell_{\text{max}}$  with  $1\sigma$  Monte Carlo bands. The Planck data lie well below the  $\Lambda$ CDM mean and its  $1\sigma$  band at all  $\ell_{\text{max}}$ . The model mean is lower and the Planck data sit within or near the model band throughout.

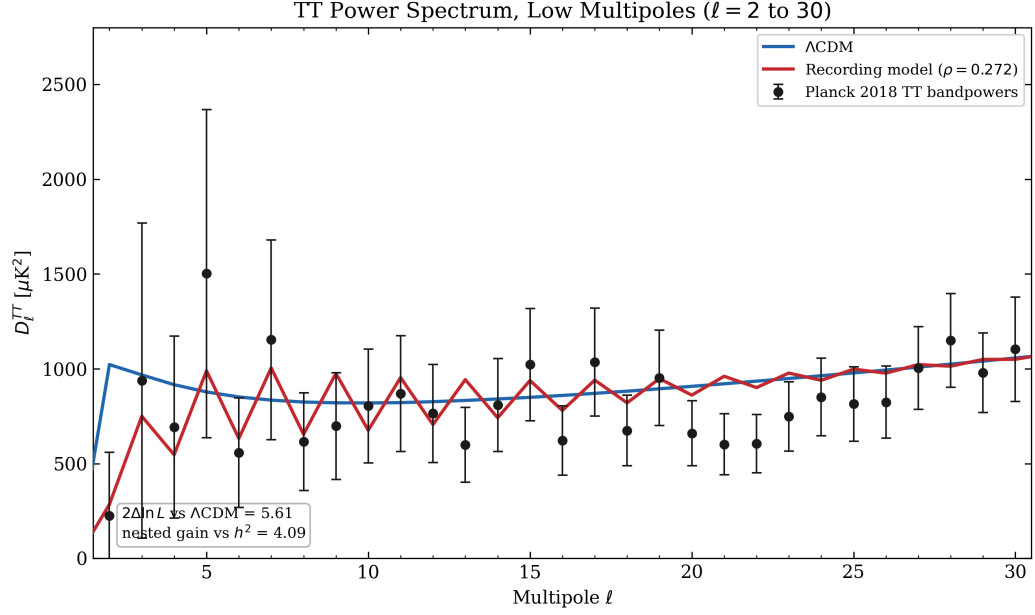


Figure 2: Low- $\ell$  TT power spectrum. Planck 2018 bandpowers (black circles),  $\Lambda\text{CDM}$  (blue), and the geometric-closure recording model (red; configuration D,  $\rho = 0.27$ ). The model produces an even/odd seesaw tracking the data while the angular recording filter suppresses  $\ell = 2-3$ .

Table 2: Parity ratio lower-tail probability  $P(R < R_{\text{obs}})$  under  $\Lambda\text{CDM}$  and the geometric-closure model (configuration D), from 200,000 Monte Carlo realisations.

$\ell_{\text{max}}$	$\Lambda\text{CDM}$	Model
5	4.5%	<b>34.1%</b>
7	1.9%	<b>26.4%</b>
10	2.4%	<b>35.2%</b>
15	3.0%	<b>53.6%</b>
20	0.8%	<b>30.5%</b>
22	0.7%	<b>30.1%</b>
25	1.2%	<b>37.7%</b>
30	2.2%	<b>44.3%</b>

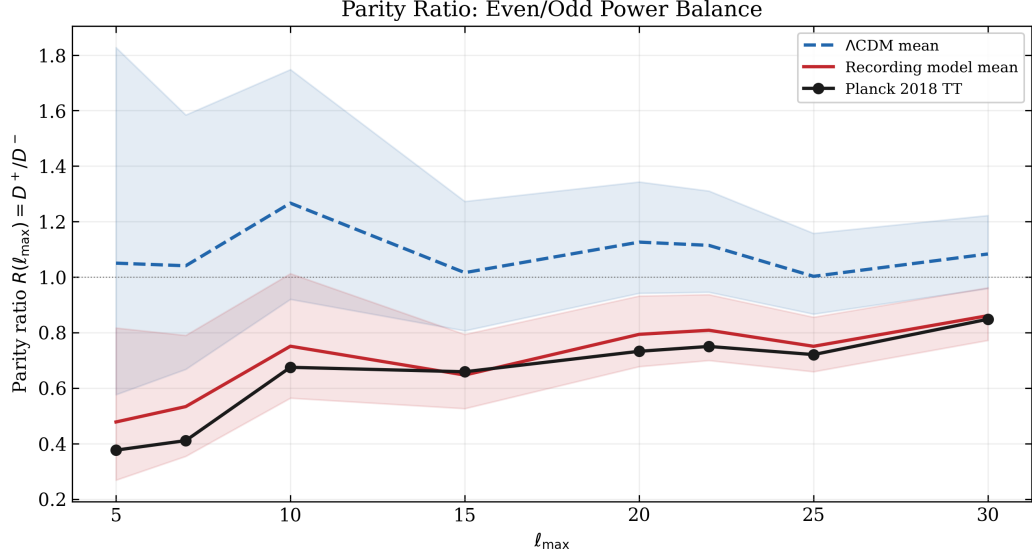


Figure 3: Parity ratio  $R(\ell_{\max}) = D^+/D^-$  as a function of  $\ell_{\max}$ . Planck 2018 (black),  $\Lambda$ CDM mean and  $1\sigma$  band (blue), geometric-closure model mean and  $1\sigma$  band (red). The Planck data lie below the  $\Lambda$ CDM expectation but are consistent with the model.

#### 4.4 Angular correlation function and $S_{1/2}$

The parity extension does not disturb the  $S_{1/2}$  resolution achieved by the angular recording filter [26]. Figure 4 shows the angular correlation function  $C(\theta)$  for  $\Lambda$ CDM, the geometric-closure model, and the Planck-derived bandpowers. The model suppresses the persistent positive tail of  $\Lambda$ CDM at  $\theta \gtrsim 60^\circ$  and tracks the Planck curve across the critical angular range.

The theoretical  $S_{1/2}$  values are:  $\Lambda$ CDM,  $34,878 \mu\text{K}^4$ ; model,  $4,484 \mu\text{K}^4$ ; Planck bandpower-derived,  $6,774 \mu\text{K}^4$ . Figure 5 shows the  $S_{1/2}$  distributions from 10,000 Monte Carlo realisations. Under  $\Lambda$ CDM, the Planck bandpower-derived  $S_{1/2}$  falls at the 8.4th percentile. Under the model, it falls at the 43.2nd percentile — typical rather than anomalous. The combined model places  $S_{1/2}$  close to the median, consistent with the angular filter result of the preceding paper [26].

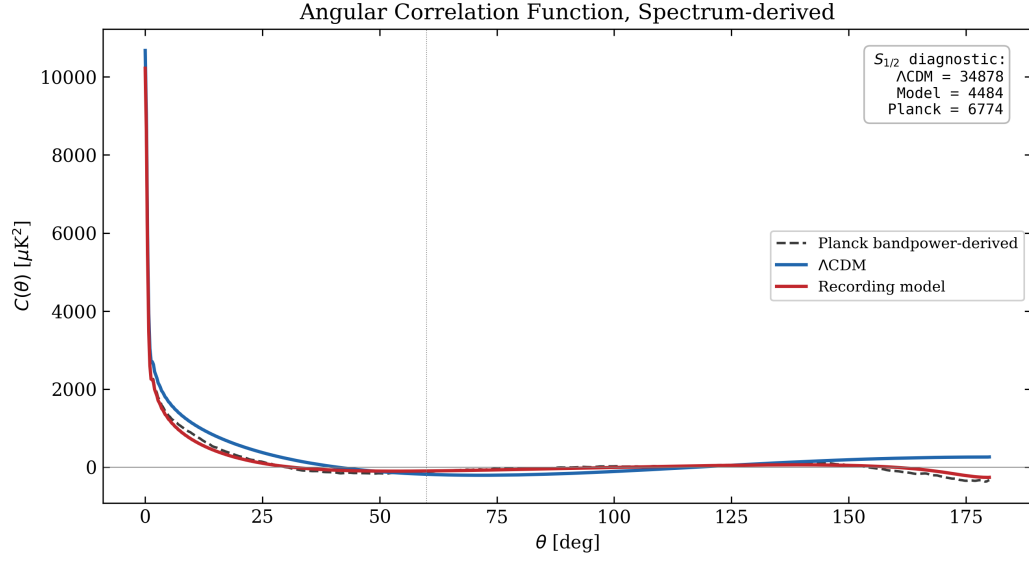


Figure 4: Angular correlation function  $C(\theta)$  for  $\Lambda$ CDM (blue), the geometric-closure model (red), and Planck 2018 bandpowers (black dashed). The vertical dotted line marks  $60^\circ$ ;  $S_{1/2}$  values are shown inset.

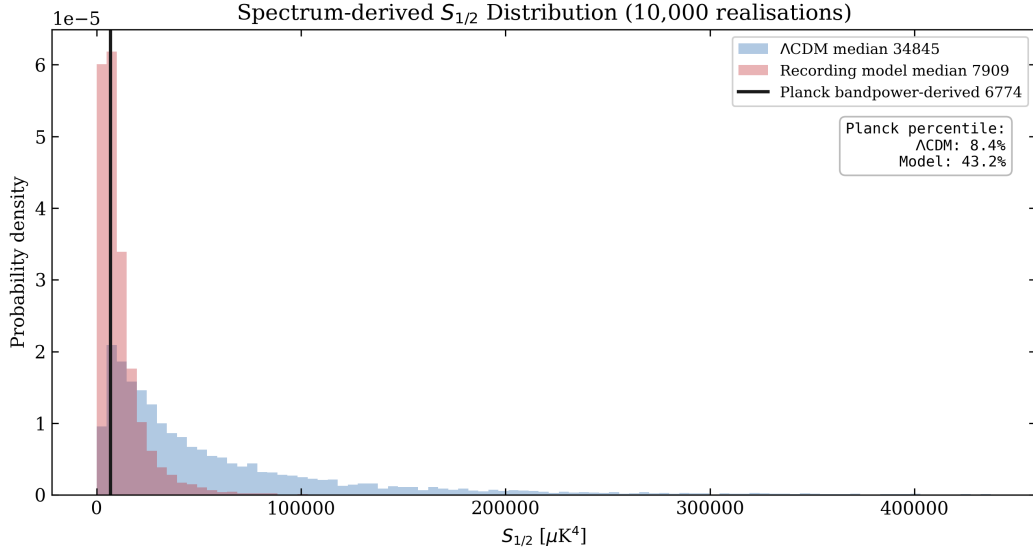


Figure 5: Distribution of  $S_{1/2}$  from 10,000 Monte Carlo realisations under  $\Lambda$ CDM (blue) and the geometric-closure model (red). The Planck-observed value (black line) falls at the 8.4th percentile of  $\Lambda$ CDM but at the 43.2nd percentile of the model.

## 5 Discussion

The PMH recording architecture introduced in this programme derives three channels from the observer’s causal diamond: an angular filter resolving the low-power anomaly, a radial kernel addressing the cosmic dipole anomaly, and a variance decoder producing the quadrupole–octopole alignment geometry [24, 29, 31]. All three draw on the unsigned firing rate, the quadratic threshold probability that erases the sign of the local fluctuation, and are therefore structurally parity-even. The present paper now identifies the missing channel that could account for the parity anomaly, being a signed evidence contrast across a diameter of the causal diamond. It is shown that the Lindblad collapse operator already carries the sign; the diamond’s modular structure supplies the antipodal pairing; the contrast is sensitive to odd- $\ell$  modes (which flip sign across the diameter) and blind to even- $\ell$  modes (which do not). Three structural closures fix the operator to  $\mathcal{O}_A = -\rho e^{\Delta s^2/L_A^2} \mathcal{P}$ , and a geometric scale closure  $L_A^2 = d(d+1)\ell_c^2 = 251.2$  reduces the model to one fitted parameter currently accounting for the missing amplitude.

A supportive finding for the new integrated model is that fixing both scale parameters from geometry costs little likelihood. The three-parameter best-fit gives  $2\Delta \ln \mathcal{L} = 5.89$ ; the one-parameter geometric closure gives 5.61 (Table 1). The geometric values remain consistent with the unconstrained optimum; fixing them costs less than 0.3 in  $2\Delta \ln \mathcal{L}$ . This extends an earlier result from the angular filter paper [26], where  $\ell_c^2 = 12.56$  was close to the earlier low- $\ell$  likelihood optimum; here the agreement is tighter and covers the second scale as well. The parity ratio diagnostic confirms that the resolution is simultaneous across all tested  $\ell_{\max}$  (Table 2), and the  $S_{1/2}$  improvement achieved by the angular filter is preserved.

The antipodal operator extends the existing architecture of the programme. It adds a classical evidence-processing step between the local quantum monitoring and the decoder: each boundary cell undergoes quantum measurement independently; the antipodal subtraction acts only on the resulting classical records. The canonical parity selection rule applies to the unsigned channel; the antipodal operator acts on a distinct signed channel. Backward compatibility is therefore preserved and the programme overall retains a coherent shape.

However, two major theoretical questions remain. First, the contrast amplitude  $\rho = 0.27$  remains the model’s sole fitted parameter. This feature extends and sharpens the problem of programme-wide ‘amplitude gap’ [23, 24]. The naive scale for recording-architecture effects is  $v/c \sim 10^{-3}$ , roughly two orders of magnitude smaller. This gap is shared with the decoder and dipole kernel amplitudes [24, 31], and its resolution is the programme’s central open problem. A first-principles derivation of  $\rho$  would eliminate the model’s last free parameter. Second, the geometric scale closure  $L_A^2 = d(d+1)\ell_c^2$  is numerically strong but currently lacks a derivation from the underlying modular dynamics. It remains a well-motivated hypothesis.

Several limitations are noted. The analysis uses an approximate per-multipole scaled- $\chi^2$  likelihood with effective  $f_{\text{sky}} = 0.86$  and does not account for inter-multipole correlations induced by the Galactic sky cut. A full masked analysis with the Planck low- $\ell$  likelihood is reserved for future work. The analysis is restricted to TT; predictions for the parity structure of the EE and TE spectra are also deferred. Finally, the structural derivation shows that *if* a signed antipodal channel is active, its form is uniquely determined, but the paper does not prove from first principles that such a channel must be active; the activation is physically motivated rather than derived. The comparison against  $\Lambda$ CDM is descriptive rather than a nested hypothesis test, because the recording model does not reduce to  $\Lambda$ CDM when  $\rho = 0$  (the angular filter  $h^2(\ell)$  remains). The proper nested test is  $h^2$ -only versus  $h^2 + \rho$ , which gives  $2\Delta \ln \mathcal{L} = 4.1$  for one boundary parameter ( $\rho \geq 0$ ) with a boundary-mixture  $p$ -value of 0.022.

In summary, the smoothed antipodal evidence operator introduced here provides a one-parameter extension of the PMH recording architecture that resolves the low- $\ell$  parity anomaly across all tested  $\ell_{\max}$  while preserving the  $S_{1/2}$  and alignment results of the existing pro-

gramme. Its three components, being the antipodal pairing, the sign, and the smoothing envelope are each fixed by a structural principle; its scale is fixed by a geometric closure; and only the contrast amplitude  $\rho$  remains fitted. Deriving that amplitude from first principles is the key open question.

## References

- [1] Wayne Hu and Scott Dodelson. Cosmic microwave background anisotropies. *Annual Review of Astronomy and Astrophysics*, 40:171–216, 2002.
- [2] Planck Collaboration. Planck 2018 results. VI. cosmological parameters. *Astronomy and Astrophysics*, 641:A6, 2020.
- [3] Dominik J. Schwarz, Craig J. Copi, Dragan Huterer, and Glenn D. Starkman. CMB anomalies after Planck. *Classical and Quantum Gravity*, 33:184001, 2016.
- [4] P. K. Aluri et al. Examining statistical isotropy of CMB low multipoles from Planck PR4 data. *Physics Letters B*, 836:137593, 2023.
- [5] M. Billi, R. B. Barreiro, and E. Martínez-González. The anomaly of the CMB power with the latest Planck data. *Journal of Cosmology and Astroparticle Physics*, 2024(07):080, 2024.
- [6] Jaiseung Kim and Pavel Naselsky. Anomalous parity asymmetry of the Wilkinson Microwave Anisotropy Probe power spectrum data at low multipoles. *Astrophys. J. Lett.*, 714:L265–L267, 2010.
- [7] Planck Collaboration, P. A. R. Ade, et al. Planck 2015 results. XVI. Isotropy and statistics of the CMB. *Astron. Astrophys.*, 594:A16, 2016.
- [8] Planck Collaboration. Planck 2018 results. VII. isotropy and statistics of the CMB. *Astronomy and Astrophysics*, 641:A7, 2020.
- [9] Jaiseung Kim and Pavel Naselsky. Anomalous parity asymmetry of WMAP 7-year power spectrum data at low multipoles: Is it cosmological or systematics? *Physical Review D*, 82(6):063002, 2010.
- [10] Craig J. Copi, Dragan Huterer, Dominik J. Schwarz, and Glenn D. Starkman. Large-angle anomalies in the CMB. *Advances in Astronomy*, 2010:847541, 2010.
- [11] Craig J. Copi, Dragan Huterer, Dominik J. Schwarz, and Glenn D. Starkman. No large-angle correlations on the non-Galactic microwave sky. *Monthly Notices of the Royal Astronomical Society*, 399:295–303, 2009.
- [12] A. de Oliveira-Costa, M. Tegmark, M. Zaldarriaga, and A. Hamilton. The significance of the largest scale CMB fluctuations in WMAP. *Physical Review D*, 69:063516, 2004.
- [13] Kate Land and João Magueijo. Examination of evidence for a preferred axis in the cosmic radiation anisotropy. *Physical Review Letters*, 95:071301, 2005.
- [14] Joann Jones, Craig J. Copi, Glenn D. Starkman, and Yashar Akrami. Strong evidence against a statistically isotropic universe. *arXiv preprint*, 2023. v3, revised March 2026; submitted to Phys. Rev. D.

- [15] Jean-Pierre Luminet, Jeffrey R. Weeks, Alain Riazuelo, Roland Lehoucq, and Jean-Philippe Uzan. Dodecahedral space topology as an explanation for weak wide-angle temperature correlations in the cosmic microwave background. *Nature*, 425:593–595, 2003.
- [16] Carlo R. Contaldi, Marco Peloso, Lev Kofman, and Andrei Linde. Suppressing the lower multipoles in the CMB anisotropies. *Journal of Cosmology and Astroparticle Physics*, 2003(07):002, 2003.
- [17] J. Liu and F. Melia. A truncated primordial power spectrum and its impact on B-mode polarization. *Physics Letters B*, 853:138645, 2024.
- [18] Enrique Gaztañaga and K. Sravan Kumar. Finding origins of CMB anomalies in the inflationary quantum fluctuations. *J. Cosmol. Astropart. Phys.*, 2024(06):001, 2024.
- [19] John A. Wheeler. The ‘past’ and the ‘delayed-choice’ double-slit experiment. In A. R. Marlow, editor, *Mathematical Foundations of Quantum Theory*, pages 9–48. Academic Press, 1978.
- [20] John A. Wheeler and Wojciech H. Zurek. *Quantum Theory and Measurement*. Princeton University Press, 1984.
- [21] Gregory O’Grady. Extending Wheeler’s participatory universe: A conceptual framework for a ‘Measurereverse’. Preprint, Zenodo. <https://doi.org/10.5281/zenodo.17956983>, 2025.
- [22] Gregory O’Grady. The ‘Participatory Horizon’: Causal limits and the CMB low power anomaly. Preprint, Zenodo. <https://doi.org/10.5281/zenodo.17946020>, 2025.
- [23] Gregory O’Grady. Kinematic participatory horizons and the axis of evil. Preprint, Zenodo. <https://doi.org/10.5281/zenodo.17922164>, 2026.
- [24] Gregory O’Grady. Participatory horizons and the cosmic dipole anomaly. Preprint, Zenodo. <https://doi.org/10.5281/zenodo.19528259>, 2026.
- [25] Gregory O’Grady. Radial participatory horizon: A nested causal-diamond framework. Preprint, Zenodo. <https://doi.org/10.5281/zenodo.19639604>, 2026.
- [26] Gregory O’Grady. The participatory horizon as an angular recording filter: A derived CMB suppression scale. Preprint, Zenodo. <https://doi.org/10.5281/zenodo.19647157>, 2026.
- [27] Gregory O’Grady. Participatory horizons and the cosmic dipole anomaly II: A cross-survey analysis. Preprint, Zenodo. <https://doi.org/10.5281/zenodo.19658674>, 2026.
- [28] Horacio Casini, Marina Huerta, and Robert C. Myers. Towards a derivation of holographic entanglement entropy. *Journal of High Energy Physics*, 2011(05):036, 2011.
- [29] Gregory O’Grady. The participatory modular Hamiltonian: Architecture for the participatory horizon programme — part I. Preprint, Zenodo. <https://doi.org/10.5281/zenodo.19713513>, 2026.
- [30] Gregory O’Grady. The participatory Lindblad equation: Architecture for the participatory horizon programme — part II. Preprint, Zenodo. <https://doi.org/10.5281/zenodo.19722842>, 2026.

- [31] Gregory O’Grady. The participatory decoder: Architecture for the participatory horizon programme — part III. Preprint, Zenodo. <https://doi.org/10.5281/zenodo.19722950>, 2026.
- [32] Antony Lewis, Anthony Challinor, and Anthony Lasenby. Efficient computation of cosmic microwave background anisotropies in closed friedmann-robertson-walker models. *Astrophysical Journal*, 538:473–476, 2000.